SIMULATION OF PLUNGER-TYPE WAVE MAKERS*

Tommi Mikkola

Journal of Structural Mechanics,
Vol. 40, No 4, 2007, pp. 19-39

SUMMARY

As a part of a wave maker renewal project unstructured, time accurate, finite volume method has been verified and used for a wave maker design problem. The method of manufactured solutions has been used for the verification of the code both for simulation of steady flows without free surface as well as time accurate free surface flows. The results show expected order of convergence in both cases. In the design problem three wedges with angles 25, 35 and 45 degrees have been considered. The performance of different wedge angles for a plunger type wave maker have been compared in terms of the height and quality of the generated wave. The results show that the wedge angle has a considerable influence on the wave height as well as on the wave quality. Increasing wedge angle increases the wave height, but at the same time the fluctuations of the asymmetries of the wave profile increase. The motion frequency has also a significant influence on the wave quality. Due to its overall performance the 35 degree wedge has been chosen for the new wave maker and a further analysis to estimate the requirements for the driving mechanism has been performed.

INTRODUCTION

The work presented here is part of an ongoing wave maker renewal project at the Ship Laboratory of Helsinki University of Technology. The original wave maker in the long towing tank of the laboratory was built nearly thirty years ago. Since then ship size has increased constantly especially for cruise ships. However, the length of a ship model is limited by the model test facility. Therefore, as the ship size increases larger model scales have to be used. On the other hand, as the model scale increases the wave lengths in model scale for sea-keeping tests decrease.

In this regard the limits of the existing wave maker in the towing tank had been reached. This was partly due to the wear and tear of the wave maker, but also due to its construction and design. It was therefore decided that the old wave maker is replaced with a modernised version based on the design of the wave maker at the multi-purpose basin of the Ship Laboratory. Similarly to the old wave maker this is a plunger type wave

*Based on papers originally presented at 26th Symposium on Naval Hydrodynamics (Mikkola, 2006) and at 10th Numerical Towing Tank Symposium (Mikkola, 2007).

maker, but with linear motion instead of the motion along a circular arc of the old wave maker.

It was decided already at an early stage of the renewal project that for the new wave maker only triangular cross sections are considered. Certain advantages are associated with the triangular shape. In addition to the simple construction, in case of triangular shape a change in the immersion depth does not change the geometry of the wave maker cross section. A controlled fine tuning of the wave maker performance is thus possible simply through adjustment of the mean position and scaling of the wave making characteristics.

The wave maker at the multi-purpose basin was designed in the early nineties using model testing and wave maker theory based on linear wave theory (Granholm, 1990). The computational method used was based on the boundary collocation method (Wu, 1988). Since then other methods applicable for simulation of wave generated by oscillating bodies have been developed. One of these methods is an unstructured finite volume solver (Yet Another Fine Flow Analyser - YAFFA) for time accurate inviscid and viscous flows developed by the author.

The work presented here consists of two parts. In the first part the method of manufactured solutions has been used to check the numerical implementation of the developed method. In the second part the solution method has been used for the wave maker design problem by comparing the performance of different wedge angles in terms of the height and quality of the generated wave. Based on these results one angle has been selected for the wave maker, and the requirements for the driving mechanism have been estimated.

The paper is organised as follows. First the numerical method used is described. Then the verification of the code is discussed followed by the design problem. The paper ends with the conclusions.

NUMERICAL METHOD

The numerical method is based on 2D unstructured Finite Volume Method (FVM). A collocated SIMPLE-type pressure correction scheme is used for the solution of the bulk flow, with velocities and pressures stored at the cell centres. Boundary conditions are implemented with a layer of ghost cells outside the computational domain. Free surface flows are simulated using a surface tracking approach. Free surface deformation is solved from the kinematic boundary condition using a semi-implicit scheme, and dynamic boundary condition is coupled to the pressure correction equation. Grid updating is performed with a linear/torsional spring analogy (Batina, 1991; Farhat et al., 1998), with a Laplacian smoothing or with a combination of these two. Solution of time accurate flows is based on a dual time step approach, in which pseudo time derivatives are added into the unsteady flow equations and solution is iterated in pseudo time for each physical time step until these additional terms vanish. Momentum equations are solved with conjugate gradient squared stabilised (CGSTAB) (van den Vorst and Sonneveld, 1990) method and the pressure correction equation with conjugate gradient (CG) (Golub and van Loan, 1990) method. In both cases incomplete Cholesky preconditioning is used.

In the following sections a more detailed description of selected parts of the method

is given. For additional details the reader is referred to (Mikkola, 2006).

Governing equations

In this work the flow is assumed to be incompressible and isothermal in 2D. Since it is assumed that viscosity does not have significant influence in the problem at hand its influence ha been neglected. The governing equations for the flow are the incompressible continuity and Euler equations. In conservation form these are

$$\begin{aligned} &\int_{\partial\Omega} \rho v_i n_i dS = 0 \ \text{ and} \\ &\frac{\partial}{\partial t}\int_{\Omega} \rho v_i dV + \int_{\partial\Omega} \rho v_i \left(v_j n_j - v_g\right) dS = -\int_{\partial\Omega} p n_i dS \end{aligned} \tag{1}$$

respectively. Here ρ is the density, v_i are the velocity components, v_g is the grid velocity normal to $\partial\Omega$ and n_i are the components of the outer normal for domain Ω. The piezometric pressure p includes the effect of gravity and is given by

$$p = p^{\text{tot}} + \rho g x_2 \ , \tag{2}$$

where p^{tot} is the total physical pressure and gravity with acceleration g points in the negative x_2-direction.

Two boundary conditions have to be satisfied on the deforming free surface. The kinematic boundary condition states that there is no flow through the interface, such that

$$\left(v_i - v_i^{\text{fs}}\right) n_i = 0 \ , \tag{3}$$

where v_i^{fs} is the velocity of the free surface.

The second condition to be satisfied on the free surface is the dynamic boundary condition. This states that stresses are continuous across the free surface. In this work, the inviscid approximation of this without surface tension effects is used. By assuming zero atmospheric pressure and taking into account Eq. (2) the dynamic boundary condition is simplified into

$$p = \rho g h \tag{4}$$

for the piezometric pressure on the free surface, where h is the wave height.

Unstructured finite volume method

In finite volume methods the computational domain is divided into non-overlapping subdomains – the finite volume grid – and Eqs. (1) are applied for each element of the grid separately. If unstructured grids are used, the volumes may be ordered arbitrarily and – regarding the ordering – only the connections between neighbours are required.

The surface integrals in the continuity and momentum balance equations for a finite volume l of the grid are written as sums over the sides lm connecting volume l to its neighbours m leading to

$$\sum_m \dot{m}_{lm} = 0 \quad \text{and} \tag{5}$$

$$\rho V_l \frac{\partial v_{i,l}}{\partial t} = -\sum_m F_{i,lm} \tag{6}$$

respectively. Here

$$\dot{m}_{lm} = \rho \bar{v}_{(lm)} S_{(lm)} \tag{7}$$

is the mass flux through face lm and $\bar{v}_{lm}$ is the convection velocity normal to the face. The inviscid flux in the momentum balance equations (6) is given by

$$\begin{aligned} F_{i,lm} = \rho v_{i,(lm)} \left(\bar{v}_{(lm)} - v_{g,(lm)} \right) S_{(lm)} + \\ + p_{(lm)} n_{i,(lm)} S_{(lm)} \ . \end{aligned} \tag{8}$$

Bulk flow solution

The bulk flow solution process is based on a velocity-pressure decoupling, in which the velocities and pressures are solved separately in an iterative manner. In each iteration, the velocity field is first updated from momentum balance (6) with time marching in pseudo time τ and using the current pressure field. The velocity is corrected after this by altering the pressure according to the resulting mass balance error in the continuity equation (5). This process is repeated in pseudo time until a steady state is reached. For time accurate flows each physical time step is considered as a steady state problem. Therefore the solution of a steady state problem is considered first. The discussion on the implementation of time accuracy is then based on the steady state formulation.

Momentum balance

Momentum equations (6) are integrated in pseudo time with the implicit Euler scheme. Linearisation of the fluxes gives

$$A_{P,l} \Delta v_{i,l} + \sum_{n \neq l} a_{ln} \Delta v_{i,n} = R_{i,l} \ , \tag{9}$$

where

$$A_{P,l} = \frac{\rho V_l}{\Delta \tau} + a_{(l)(l)} \qquad a_{ln} = \sum_m \frac{\partial F_{i,lm}}{\partial v_{i,n}} \tag{10}$$

are the diagonal and off-diagonal terms respectively and

$$R_{i,l} = -\sum_m F_{i,lm} \tag{11}$$

is the explicit residual.

The convected velocity components $v_{i,lm}$ are upwinded by

$$v_{i,lm} = v_{i,l} + \frac{\partial v_{i,l}}{\partial x_i} \left(x^{\mathrm{c}}_{i,lm} - x_{i,l} \right) \ , \tag{12}$$

where the flow is assumed to be from l to m. Above $x^{\mathrm{c}}_{i,lm}$ are the coordinates of the centre of the face.

The convection velocity $\bar{v}_{lm}$ and the pressure p_{lm} in Eq. (8) are taken as distance weighted averages of the values at auxiliary points l' and m'. The points are projected from points l and m respectively on a line normal to face lm and going through the centre point of this face. The values at the auxiliary points are evaluated with first order Taylor extrapolation using a gradient averaged on the corresponding face. The gradient components for velocities and pressure, required for the extrapolations, are calculated using a least squares based method described in e.g. (Demirdžić and Muzaferija, 1995).

The grid velocity $v_{g,lm}$ in Eq. (8) is based on the geometric conservation law (Hoffren, 1993). For each face it is associated with the volume swept by the face between time steps.

In the implicit stage, i.e. for the calculation of the linearised terms in (10), the fluxes are approximated with first order schemes. This ensures that only the closest neighbours of a volume contribute to the linear system (9).

Mass balance and pressure correction

If the velocities resulting from the momentum equations do not satisfy the continuity condition, the flow field has to be corrected. The corrected velocities can be written as

$$v_i = v_i^* + v_i' \qquad p = p^* + p' \tag{13}$$

Here, v_i^* and p^* are the provisional velocity components and pressure after the solution of the momentum equations and v_i' and p' are the unknown corrections. Continuity condition (5) for the corrected velocities gives a relation between the provisional values and the corrections

$$\sum_m \dot{m}_{lm}' = -\sum_m \dot{m}_{lm}^* \tag{14}$$

In order to avoid decoupling of the neighbouring velocities and pressures, some artificial damping must be added into the mass fluxes in the mass balance error in Eq. (14). In the current method a damping term d_{lm} similar to the ones proposed by Rhie and Chow (1983) and Davidson (1996) is used. With the added damping, the mass flux on a face can be written as

$$\dot{m}_{lm}^* = \rho S_{(lm)} \bar{v}_{(lm)}^* + C \frac{\rho S_{(lm)}^2}{A_{P,(lm)}} d_{lm} \,, \tag{15}$$

where C is a parameter controlling the amount of damping and $A_{P,lm}$ is the average of the diagonal terms $A_{P,l}$ and $A_{P,m}$.

The connection between the change of pressure and mass flux on a face can be derived from the momentum equations. The approach used in the SIMPLE method (Caretto et al., 1972) gives the pressure correction equation

$$\sum_m \alpha_{lm} p_m' = -\sum_m \dot{m}_{lm}^* \,. \tag{16}$$

Here

$$\alpha_{lm} = -\frac{\rho S_{lm} V_{lm}}{A_{P,lm}' n_{i,lm} \left(x_{i,m} - x_{i,l}\right)} \qquad \alpha_{ll} = -\sum_{m \neq l} \alpha_{lm} \tag{17}$$

are the off-diagonal and diagonal elements respectively. V_{lm} and $A'_{P,lm}$ are taken as averages of the values on both sides of the face with $A'_{P,l}$ and $A'_{P,m}$ based on the SIMPLEC algorithm (van Doormal and Raithby, 1984).

Updated pressures and velocities are given by

$$p_l^{k+1} = p_l^k + \alpha_p p'_l \qquad v_{i,l}^{k+1} = v_{i,l}^* + \alpha_v v'_{i,l} \; , \tag{18}$$

where α_p and α_v are under-relaxation factors. Velocity corrections are calculated from

$$A'_{P,l} v'_{i,l} = -\sum_m S_{lm} p'_{lm} n_{i,lm} \; . \tag{19}$$

Time accurate bulk flow solution

The simulation of time dependent flows is based on a three level fully implicit scheme (3-LFI) (Hoffren, 1993). The method is implemented using dual time stepping, i.e. two time steps – a physical and a pseudo one – are used. This is done by including the physical time derivative terms into the appropriate time-marching steady state equations and keeping the pseudo time derivative terms. Within each physical time step, the problem is considered as a steady state problem and is iterated until the pseudo time derivative terms vanish.

For the bulk flow we start with the implicit time-marching steady state momentum equations

$$\frac{V \Delta v_i^k}{\Delta \tau} = R_i^{k+1} \; , \tag{20}$$

where k is the pseudo iteration step. Including a three level difference approximation for the physical time derivative (Hoffren, 1993) on the left hand side of this equation leads to

$$\begin{aligned} \frac{3V^{n+1} v_i^{n+1} - 4V^n v_i^n + V^{n-1} v_i^{n-1}}{2\Delta t} + \\ + \frac{V^k \Delta v_i^k}{\Delta \tau} = R_i^{k+1} \; , \end{aligned} \tag{21}$$

where n is the physical iteration step. By approximating the future physical values by values at the next pseudo iteration Eq. (21) can be written as

$$\begin{aligned} V^{n+1,k} \left(\frac{3}{2\Delta t} + \frac{1}{\Delta \tau} \right) \Delta v_i^{n+1,k} = R^{n+1,k+1} + \\ - \frac{3V^{n+1,k} v_i^{n+1,k} - 4V^n v_i^n + V^{n-1} v_i^{n-1}}{2\Delta t} \; . \end{aligned} \tag{22}$$

Free surface solution

Time accurate free surface boundary condition

A common approach with surface tracking methods is to only solve for the vertical movement of the free surface. In order to avoid some of the drawbacks of this approach – especially with extremely steep waves – the free surface is defined as a parametric curve $(h_x(s), h_y(s))$ deforming in the direction of the free surface normals. In the dual time

stepping approach used the deformation of the free surface is solved from the kinematic boundary condition as

$$\frac{\partial h_i}{\partial \tau^{\mathrm{fs}}} = v_n n_i - \frac{\partial h_i}{\partial t} \,, \tag{23}$$

where h_i are the components of the free surface location defined at the centre of a free surface face. The deformations $\Delta h_i = \Delta h_n n_i$, with Δh_n being the deformation in the normal direction. τ^{fs} is the free surface pseudo time, n_i are the components of the outward directed normal vector on a free surface face and $v_n = v_i n_i$ is the normal velocity on the free surface. It should be noted that the free surface pseudo time step does not have to be equal to the bulk flow pseudo time step. For each physical time step (Δt) this equation is iterated with the momentum and pressure correction equations in pseudo time (with $\Delta \tau^{\mathrm{fs}}$) until a steady state is reached.

The implementation of the kinematic boundary condition can be divided into two parts: the discretisation of the normal component of the particle velocity on the free surface and the discretisation of the velocity of the bounding surface. The former constitutes the steady state part of the equation. The latter has, in principle, significance only in time accurate simulations, as in steady state the velocity of the surface vanishes. The corresponding discretisations will be discussed next.

Discretisation of the normal and the surface velocities

Several authors have suggested that some numerical damping is included in the kinematic free surface condition by up-winding the slope of the free surface (see e.g. (Hino et al., 1993), (Raven et al., 2004)). Similarly, in this work optional, controlled, numerical damping is added into Eq. (23) through up-winding in the first term on the right hand side of the equation, i.e. the normal velocity. Namely, by a simple manipulation of the first term the equation can be written as

$$\frac{\partial h_i}{\partial \tau^{\mathrm{fs}}} = v_i - v_t \frac{\partial h_i}{\partial s} - \frac{\partial h_i}{\partial t} \,, \tag{24}$$

where v_t is the tangential velocity component on the free surface. The second term on the right hand side is in a form of a convection term. Numerical damping can be introduced into the equation by up-winding the free surface slope $\partial h_i / \partial s$ in this term according to the direction of the tangential velocity.

In the current method the slope components $\partial h_i / \partial s$ in Eq. (24) are calculated by MUSCL-interpolation of the free surface coordinates. The slope of the grid may be slightly different, as grid points are always taken as weighted averages of neighbouring wave coordinates. Even though the slope calculation is based on MUSCL-approach, one should bear in mind, that this does not rule out the possibility to use central differencing for the slope components as well. By an appropriate choice of the MUSCL-parameter the scheme reduces to the central difference.

An essential part in the time accurate solution of free surface flows is the approximation of the last term in Eq. (23) representing the velocity of the free surface. (Mikkola, 2005) In the approach used here the last term in Eq. (23) is replaced directly with the

three level difference approximation for the time derivative, that is

$$\frac{\partial h_i}{\partial t} = \frac{1}{\Delta t}\left(\frac{3}{2}h_i^{n+1} - 2h_i^n + \frac{1}{2}h_i^{n-1}\right) . \tag{25}$$

CODE VERIFICATION WITH METHOD OF MANUFACTURED SOLUTIONS

In the previous section a theoretical presentation of the discretised approach for the solution of the governing equations has been given. For practical purposes the approach is implemented as a computer code. The purpose of code verification is to demonstrate that the implementation is correct in a sense that the code is solving the governing equations correctly.

In this paper the definition for Verification and Validation advocated by e.g. Roache (2002) and Salari and Knupp (2000) is adopted. Here Verification is concerned with solving the equations right and Validation with solving the right equations. With this definition Verification is purely a mathematical exercise and does not deal with the correctness of the equations in terms of physical laws. The latter is dealt with by Validation.

Roache (1998) states that verification is about solving the given partial differential equations with given boundary conditions consistently, i.e. as a measure related to the discretisation, such as the cell size or time step, approaches zero the numerical solution approaches the corresponding continuum solution. Furthermore, based on the discretisation used one usually knows the order at which the error should approach zero.

Verification is further divided into two parts: Verification of Codes and Verification of Calculations. The former deals with error evaluation using a known solution, whereas the latter deals with estimation of the error of a numerical solution. To avoid confusion Salari and Knupp (2000) recommend that the term Solution Accuracy Assessment (SAA) is used for the latter. For a code it is sufficient to perform Verification of Code just once, but after modifications the verification has to be repeated (Salari and Knupp, 2000).

The code verification process obviously requires the knowledge of the continuum solution. The best solution for comparison is an exact analytical solution for a problem. However, analytical solutions for the Euler or the Navier-Stokes equations exist only for very simplified problems. With free surface included additional complication is introduced by the non-linearity of the free surface boundary condition. This problem of lack of analytical solutions can be circumvented by using the Method of Manufactured Solutions (MMS) first presented by Steinberg and Roache (1985). Here the governing equations are modified with source terms such that a known, exact, analytical solution exists for the modified equations. In the presented work MMS has been applied for the study of the behaviour of the discretisation error of the developed method.

All of the verification results presented in the following have been simulated with double precision (64-bit). Each time step has been iterated in pseudo-time until the L_{inf}-norm of the change of the flow variables between iterations has reduced to machine zero. This removes the influence of the iteration error due to incomplete convergence (see e.g. Eça and Hoekstra, 2006). Thus, the numerical error consists only of the discretisation and round-off errors. With double precision the latter is negligible in comparison.

Method of manufactured solution

The basic idea behind MMS is to start off with the solution rather than with the equations to be solved. That is, a solution is first manufactured and the equations are then modified by adding source terms to provide the given solution. This apparently complex procedure is in fact straightforward and simple to perform, wherein lies the elegance of the method.

The necessary steps in MMS are briefly described in the following. For a more thorough explanation with some examples the reader is referred to e.g. (Roache, 2002). In MMS one starts by taking a suitable analytical solution, i.e. the manufactured solution, and substitutes it into the original governing continuum equations. If the solution does not satisfy the equations a residual is left over from the substitution. The modified equations are produced by substituting a source term equal to this residual into the original equations with the manufactured solution now satisfying these modified equations. The boundary conditions are provided by the manufactured solution or the applied boundary conditions should be combatible with the manufactured solution.

The modifications in the equations, i.e. in practise just the source terms, are then implemented into the solver in question. Solution of the modified equations with the solver gives a numerical approximation of the manufactured solution. The accuracy of the approximation depends on the discretisations of the equations and the corresponding discretisation parameters, such as cell size. Code verification can now be based on the comparison of the numerical solution and the known analytical solution. As the discretisation parameters are reduced the numerical solution should approach the analytical continuum solution. The coupling of manufactured solutions with mesh refinements for the estimation of the order of accuracy and, thus for more thorough code verification, was first presented by Steinberg and Roache (1985).

Roache (2002) and Salari and Knupp (2000) have presented some remarks on the choice of the manufactured solution. Firstly, the solution should not be trivial. On the other hand, the solution does not have to be physical either. In fact, some physical solutions, such as those for the Poiseuille or Couette flows, are undesirable as they do not activate the advection terms in the equations. Namely, one requirement for the solution is that it exercises all terms being tested in the equations. Roache (2002) further adds that one wants a solution, which exercises also all ordered derivatives in the error expansion.

Grid refinement

Two approaches have been used for the generation of the grids for the refinement studies. In the first option each grid has been generated separately with Delaundo grid generator (Müller, 1996) based on the frontal Delaunay method. Delaundo takes as input the point distribution on the boundaries and some parameters controlling the grid generation procedure. The refinement has been applied for the boundary point distributions, and the same control parameters have been used for each grid to maximise geometrical similarity of the grids. In the second approach a base grid has first been generated with Delaundo. The refined grids have been generated from this grid sequentially by bisecting each edge of the grid and dividing each triangle into four triangles with the same shape.

Verification of the spatial discretisation

Before studying the behaviour of the numerical error in the case of time accurate free surface flow solution the spatial discretisation of the bulk flow equations has been verified. For the verification the manufactured solution presented by Salari and Knupp (2000) has been used. Here the velocities and pressure are given by

$$u(x,y) = u_0 \left[\sin(x^2+y^2)\right] \quad (26)$$

$$v(x,y) = v_0 \left[\cos(x^2+y^2)\right] \quad (27)$$

$$p(x,y) = p_0 \left[\sin(x^2+y^2)+2\right] \quad (28)$$

The resulting source terms are presented in (Salari and Knupp, 2000) and have been left out for brevity. The rectangular solution domain is the same as the one used by Salari and Knupp, i.e. x is between -0.1 and 0.7 and y is between 0.2 and 0.8. Similarly, the same number of points on the boundaries has been used. However, the corresponding numbers of elements are considerably higher than in their case as in this work triangles have been used. Two different sets of grids have been used. In Set A each grid has been generated separately with Delaundo. In Set B the coarsest grid from Set A has been used as the base grid for the refinement approach.

For the numerical solution fixed velocity and extrapolated pressure has been used on the left hand and bottom boundaries, whereas fixed pressure and extrapolated velocity has been applied on the right hand and top boundaries.

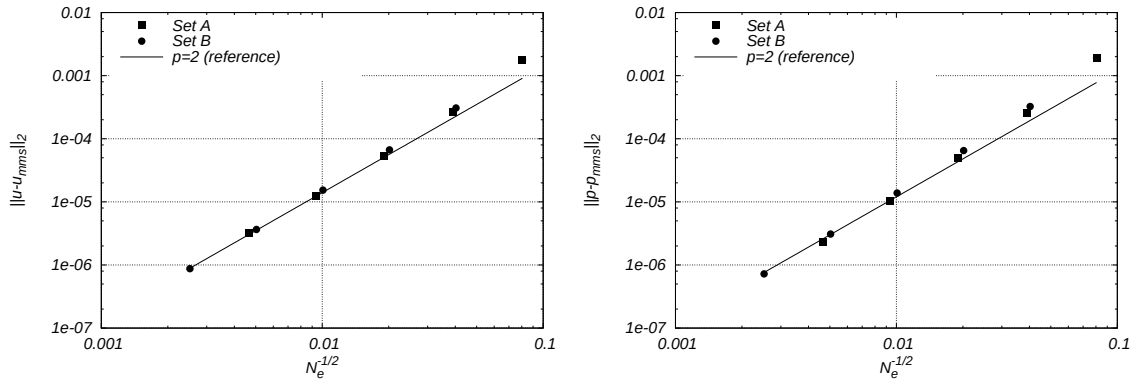

Figure 1: Verification of the spatial discretisation of the bulk flow equations using the test case by Salari and Knupp (2000). The L2-norms of the error in numerical solution as functions of generalised cell size.

Fig. 1 shows, how the numerical error – i.e. the difference between the numerical and manufactured solution – behaves as a function of a generalised measure of the cell size. Here the measure is taken as the inverse of the square root of the number of elements. The results show second-order accuracy for both the velocity and pressure as the asymptotic range is approached. This is expected as the implementation is believed to be second order accurate and thus the method is verified in this respect. It can also be seen that both approaches for grid refinement give similar results.

Verification of the time accurate free surface solution

The manufactured solution used in this study is the linearised potential flow solution for a standing wave in a rectangular container. The flow field (u, v, p) and the free surface shape ζ are given by (Paterson, 1983)

$$u(x,y,t) = \frac{\zeta_0\omega}{\sinh(kh)}\cosh[k(y+h)]\sin(kx)\sin(\omega t) \quad (29)$$

$$v(x,y,t) = -\frac{\zeta_0\omega}{\sinh(kh)}\sinh[k(y+h)]\cos(kx)\sin(\omega t) \quad (30)$$

$$p(x,y,t) = \frac{\rho g\zeta_0}{\cosh(kh)}\cosh[k(y+h)]\cos(kx)\cos(\omega t) \quad (31)$$

$$\zeta(x,t) = \zeta_0\cos(kx)\cos(\omega t) \quad (32)$$

Here $k = m\pi/L$, $\omega^2 = gk\tanh(kh)$, h is the depth of the container, L is the length of the container and m is an integer constant. In this work $h = 1.6$, $L = 40$, $\zeta_0 = 0.2$ and $m = 4$ giving two waves over the length of the tank. Based on the manufactured solution mirror boundary condition has been applied on the vertical sides of the container and slip boundary condition is used for the bottom.

The source terms are produced simply by substituting the manufactured solution given by Eqs. (29)-(32) into the governing equations. In this case the equations are the Euler equations, the continuity condition as well as the kinematic and dynamic boundary conditions

$$\frac{\partial u}{\partial t} + u\frac{\partial u}{\partial x} + v\frac{\partial u}{\partial y} + u\frac{\partial u}{\partial x} + u\frac{\partial v}{\partial y} = -\frac{1}{\rho}\frac{\partial p}{\partial x} \quad (33)$$

$$\frac{\partial v}{\partial t} + u\frac{\partial v}{\partial x} + v\frac{\partial v}{\partial y} + v\frac{\partial u}{\partial x} + v\frac{\partial v}{\partial y} = -\frac{1}{\rho}\frac{\partial p}{\partial y} \quad (34)$$

$$\frac{\partial u}{\partial x} + \frac{\partial v}{\partial y} = 0 \quad (35)$$

$$\left[1 + \left(\frac{\partial \zeta}{\partial x}\right)^2\right]^{-1/2}\left(\frac{\partial \zeta}{\partial t} + u\frac{\partial \zeta}{\partial x} - v\right) = 0 \quad (36)$$

$$p|_{fs} - \rho g\zeta = 0 \quad (37)$$

The substitution gives the following source terms for the above equations.

$$Q_u = \frac{\zeta_0^2 gk^2}{\sinh(2kh)}\sin^2(\omega t)\sin(2kx) \quad (38)$$

$$Q_v = \frac{\zeta_0^2 gk^2}{\sinh(2kh)}\sin^2(\omega t)\sinh[2k(y+h)] \quad (39)$$

$$Q_m = 0 \quad (40)$$

$$Q_{kin} = -\frac{\zeta_0\omega\sin(\omega t)}{\sinh(kh)\sqrt{1+[\zeta_0 k\sin(kx)\cos(\omega t)]^2}}(\cos(kx)\sinh(kh) \quad (41)$$

$$- \cos(kx)\sinh\left[k(h+\zeta_{ms})\right] + \zeta_0 k\sin^2(kx)\cos(\omega t)\cosh\left[k(h+\zeta_{ms})\right]\Big) \quad (42)$$

$$Q_{dyn} = \rho g\zeta_{ms}\left[\cosh(k\zeta_{ms}) + \sinh(k\zeta_{ms})\tanh(kh) - 1\right] \quad (43)$$

Here ζ_{ms} is the wave height (32) from the manufactured solution. The source term for the continuity condition vanishes as the potential flow solution itself is based on the satisfaction of the continuity condition. The source terms for the momentum equations are produced purely by the advection terms as the manufactured pressure is such that the pressure gradient cancels the inertia terms. The finite volume integrals of these source terms are approximated in the solver using the value of the source term at the geometric centre of each finite volume.

The case has been simulated with five grids and six time steps over one oscillation period. For the boundary nodes a refinement factor $r = \sqrt{2}$ has been used. The number of faces on the free surface N_{fs} and the total number of elements N_e for the different grids are given in Tab. 1. The number of time steps per one period N_T is given in the same table.

Level	0	1	2	3	4	5
N_{fs}	-	1000	706	500	353	250
N_e	-	33630	17040	8320	4243	1980
N_T	284	200	142	100	71	50

Table 1: The number of free surface faces and the total number of elements as well as the number of time steps per one oscillation period for different cell size and time step refinement levels.

For the analysis the spatial wave at each time step has been Fourier analysed. The first harmonic frequency used corresponds to the length of the manufactured wave. The analysis presented here is based on the study of the time evolution of this first harmonic component of the wave, i.e.

$$\zeta(x,t) = \zeta^1(t)\cos(kx) \tag{44}$$

For the study of the numerical damping and phase error the time variation of the first harmonic component is represented as an exponentially decaying harmonic function

$$\zeta^1(t) = \zeta_0 e^{-\alpha t}\cos(\omega t) \tag{45}$$

The damping factor α and the frequency ω are solved by nonlinear fit of the function to the numerical solutions. The results of the fit are shown for different levels of grid refinement and time step in Fig. 2. The results show clearly that – in terms of the properties of the first harmonic – the numerical solution approaches the manufactured solution as the cell size and time step approach zero. It can also be observed that the phase error is nearly independent of the cell size within the tested range.

With unsteady cases the manufactured solution can only be reached if both the cell size and the time step approach zero at the same time. Fig. 3 shows the numerical error for the damping factor and the frequency as the grid and time step are refined with the same ratio. Again, the results show the expected order of accuracy for both the damping and the phase error.

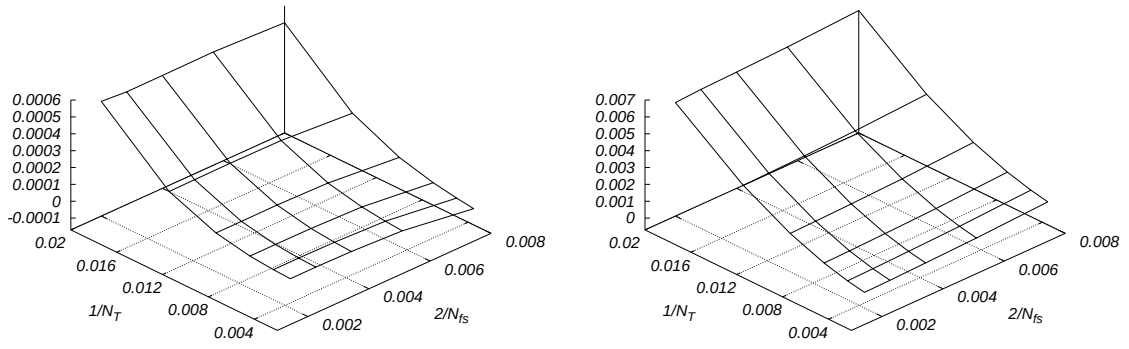

Figure 2: Discretisation error as a function of discretisation parameters. On left: damping factor α, on right: frequency ω.

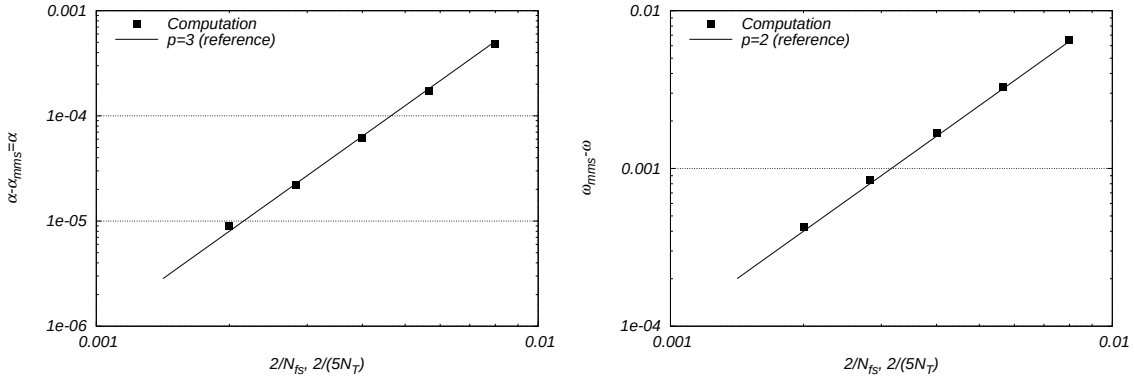

Figure 3: Numerical error with the grid and time step refined at the same time. On left: damping factor α, on right: frequency ω.

WAVE MAKER DESIGN PROBLEM

One purpose of the design problem has been to compare the performance of a triangular plunger type wave maker with different wedge angles in terms of the height and quality of the generated wave. Three wedges with angles of 25, 35 and 45 degrees with the vertical have been chosen. The water line breadth is the same (575 mm) for all three wedges.

The quality of the generated wave has been assessed primarily by studying the horizontal and vertical asymmetries of the waves. The horizontal asymmetry is defined as the ratio of the height of the crest above the zero level to the wave height. The vertical asymmetry is the ratio of the horizontal distances from the crest to the zero crossings in front of and behind the crest. The quality assessment has been done in both space and time by analysing the fluctuations of the asymmetries of the wave geometries during a motion cycle.

The setup of the design problem is illustrated in Fig. 4. The free surface boundary has been divided into two parts with damping zone from $x = 50$ m to the right hand wall. On the damping part first order upwinding is used for the wave slope in the kinematic

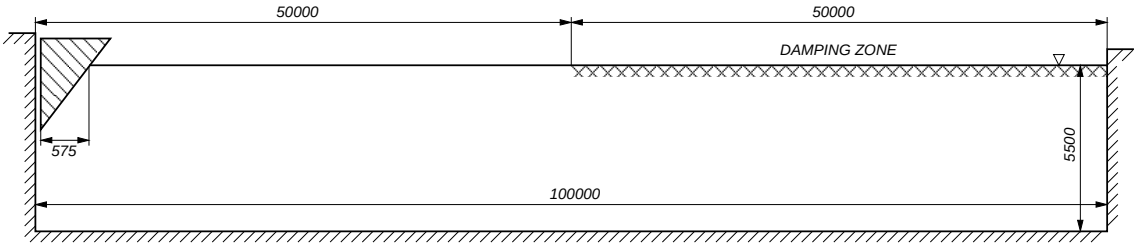

Figure 4: The wave maker design problem. Not in scale.

boundary condition.

A single grid has been generated for the case using Delaundo grid generator. The face size changes linearly between predefined sizing stations. For the wedge these are at the boundary endpoints and midpoint with sizes 0.03 m, 0.03 m and 0.05 m starting from the free surface intersection. On the free surface, the face size grows from 0.03 m at the intesection to 0.05 m at 20.115 m, stays constant up till 40 m, grows linearly to 1.0 m at 50 m and stays constant for the rest of the free surface. The size distribution on the free surface has been based on previous studies with similar cases (Mikkola, 2006). It is such that up till 40 m from the wave maker there are at least 30 points per wave length upto a motion frequency of around 6.5 rad/s. Close to the wave maker the resolution is slightly higher in order to get reliable force prediction also for higher frequencies.

The resulting grids have 27581, 26878 and 26513 elements with the 25, 35 and 45 degree wedges respectively. The corresponding numbers of faces on the wedge are 40, 29 and 24. The number of faces on the free surface for all of the cases is 897 for the part up to $x = 40$ m and 84 for the rest of the free surface up to the right hand wall. As the flow has been assumed inviscid, slip type boundary conditions have been applied on all solid boundaries, i.e. on the wedge, on the tank floor and on the vertical walls.

The simulations have been performed for four different motion amplitudes and five to nine different periods with 100 time steps per an oscillation period. The amplitude A has ranged from 25 to 200 mm and the frequency ω from 1 to 9 rad/s.

Based on the performance comparison one of the wedges has been selected for additional analysis, in order to estimate the maximum force and power requirements for the traversing gear of the wave maker. This information has also been used in the project for structural design of the wave maker. The selection of the wedge and the estimation of the power requirements are discussed separately below.

Selection of the wedge angle

The comparison of the performance of different wedge angles has been based on the study of the generated wave height, asymmetries of the wave geometry in space and the corresponding fluctuations during a motion cycle. These have been resolved by analysing ten instantaneous wave profiles over one cycle for each amplitude-period combination. Individual waves between zero-crossings have first been searched for. After this each individual wave has been processed to find the wave height as well as horizontal and vertical asymmetries.

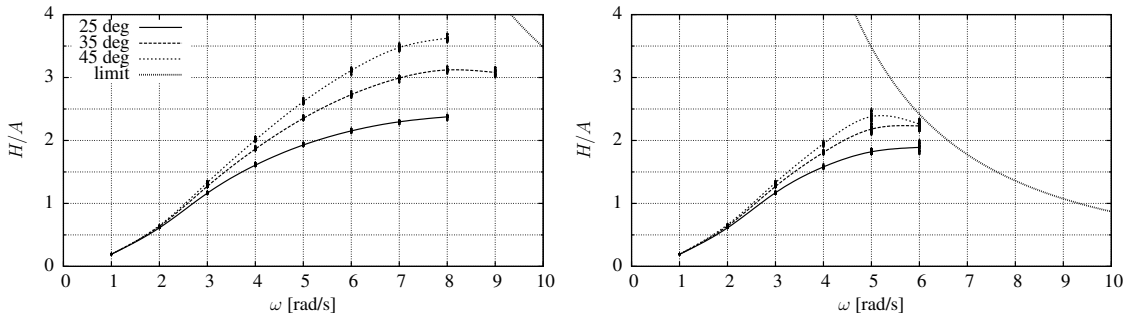

Figure 5: Comparison of the wave height H generated with different wedge angles for two motion amplitudes: $A = 25$ mm and $A = 100$ mm above and below respectively. The wave breaking limit is based on the wave length from the linear wave theory.

Fig. 5 compares the wave heights and their fluctuations with different wedge angles for two motion periods. The curves in the figures are based on the average of the fluctuating wave heights. As has been expected, the results show that a larger wedge angle leads to larger waves. This is mainly explained by the larger change in the displaced volume with increasing wedge angle. The relative difference between wedges becomes smaller with decreasing motion frequency. There is also a clear increase in the relative fluctuations as the wave slope approaches the breaking limit. However, results close to the breaking limit are questionable as wave breaking is not modelled accurately. Even if, in theory, the method is able to predict the inception of wave over-turning, the resolution of the grid is probably not sufficient to capture the high curvature of a breaking wave. An insufficient grid resolution leads to excessive numerical damping, which suppresses wave breaking and reduces local wave height. Thus, close to the breaking limit the current results may predict erroneously non-breaking waves and under-predict the wave height.

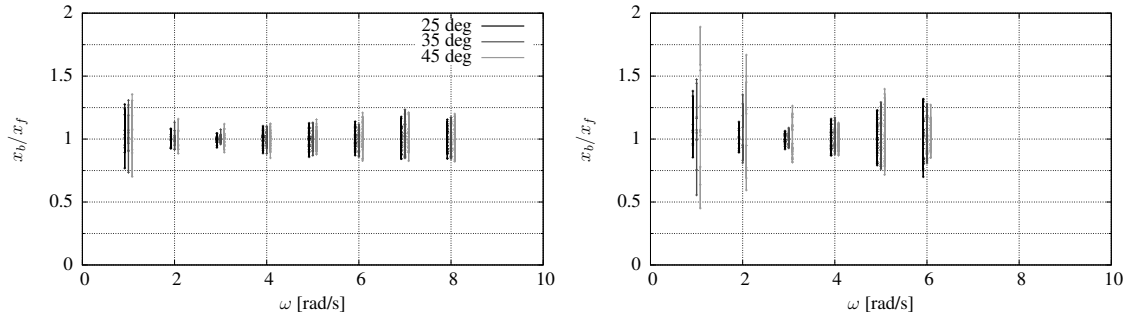

Figure 6: Comparison of the fluctuation of the vertical asymmetry of the wave profile with different wedge angles for two motion amplitudes: $A = 25$ mm and $A = 100$ mm on left and right respectively. x_b and x_f are the horizontal distances from the wave crest to the zero-crossing behind and in front of the crest respectively.

Figs. 6 and 7 compare the asymmetries between the wedges. The horizontal asymmetry is also compared with second order Stokesian approximation (Méhauté, 1976). The asymmetries characterise the geometry of the wave. For a wave with symmetric wave crests the vertical asymmetry is 1. For a wave with equal depth of through and height of

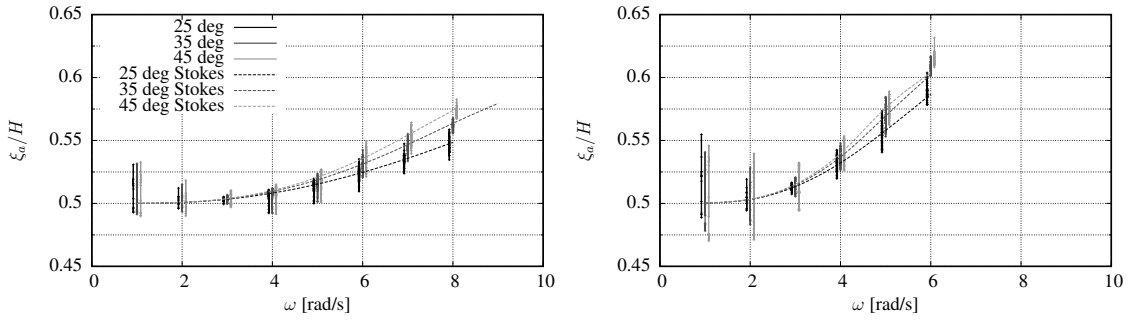

Figure 7: Comparison of the fluctuation of the horizontal asymmetry of the wave profile with different wedge angles for two motion amplitudes: $A = 25$ mm and $A = 100$ mm on left and right respectively. ξ_a is the amplitude of the wave above the still water level. Second order Stokes approximation is based on the simulated wave height.

crest from the still water level the horizontal asymmetry is 0.5. If the wave propagates with a constant geometry, the asymmetries have constant values. As can be seen from the figures, this is not the case for the generated waves. Moreover, in addition to the differences in the generated wave height between different wedge angles, there are considerable differences in the quality of the produced wave – especially in terms of the variation of the vertical asymmetry. Horizontal asymmetry does show similar differences, but in a smaller scale.

It can be roughly stated, that with the tested geometries increasing wedge angle results into increasing fluctuations of the wave geometry and thus decreasing quality of the wave. Differences are especially large for longer waves and larger motion amplitudes. The variation of the asymmetry for all the tested wedges is also highly dependent on the motion frequency. There is a clear optimal area for each wedge, where the variation of the vertical asymmetry is at its minimum. The corresponding frequency increases slightly with increasing wedge angle.

The horizontal asymmetry agrees – in average sense – rather well with the second order Stokes approximation. Slightly larger differences are observed for the higher frequencies as the motion amplitude is increased. However, as was mentioned already above, these results should be taken with caution due to possible wave breaking.

When choosing the wedge angle for the wave maker, a compromise between the wave quality and the wave height has been made. The largest wedge angle has the highest wave height to motion amplitude ratio. However, it has also the highest level of asymmetry fluctuations and has therefore been left out of the further consideration. The smallest wedge angle has the smallest asymmetry fluctuations, but requires significantly larger motion amplitudes to produce comparable wave height. The larger motion amplitude would, however, be problematic from the point of view of the mechanical construction of the wave maker – e.g. the pistons should be longer, in addition to which the piston arms should be thicker to prevent buckling under full loading. It was, therefore, decided that the 35 degree wedge would be used in the new wave maker. The performance in terms of generated wave height is significantly better than that of the 25 degree wedge. On the other hand, considerable differences in the quality of the generated wave compared to the

smallest wedge angle occur only for the long wave lengths, which are considered to be of lesser importance.

Requirements for the driving gear

For the sizing of the traversing gear and structural analysis of the wedge structure the force time histories for the 35 degree wedge have been Fourier analysed. The linear force coefficients as well as the second and third order force coefficients are shown in Fig. 8. The instantaneous buoyancy relative to the still water level is removed from the force prior to the Fourier analysis.

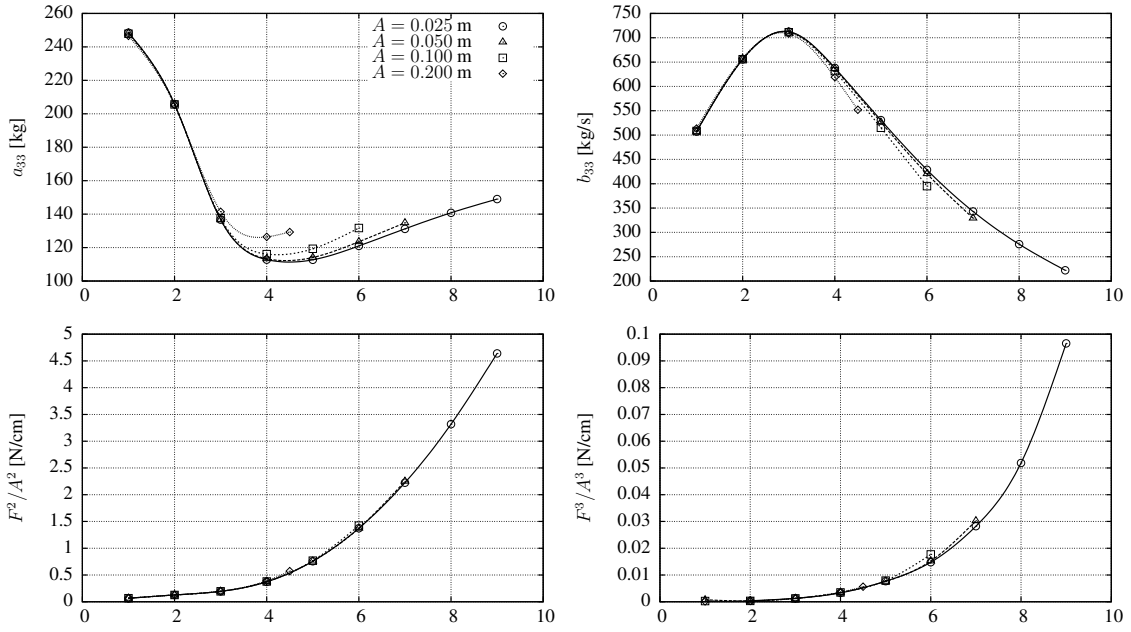

Figure 8: The added mass, damping, second order and third order coefficients for the 35 degree wedge with different motion amplitudes. The values are for a one metre long wedge with water line breadth of 0.575 m.

The added mass shows a growing motion amplitude dependency as the frequency is increased. Similar behaviour is also observed for the damping coefficient, but this might be caused by underestimation of the wave height close to wave breaking as was discussed before. Based on the results for constant frequency the second order force amplitude is very accurately a function of the square of the motion amplitude and third order force amplitude a function of the cube of the motion amplitude.

The information from the Fourier analysis combined with the mechanical limitations and the limit for breaking waves on the motion amplitude has then been used to estimate the maximum force required from the driving mechanism. The maximum absolute value of the dynamic force for different motion frequencies together with the restricted motion amplitudes are shown in Fig. 9. The dynamic force is defined here as the total force required to move the wedge minus the static net buoyancy (lift minus weight) of the wedge. The results have been scaled for the final wave maker, which is geometrically

identical to the simulated wave maker, but is one and a half times larger. As the mass of the final design is unknown at the time of writing, results for three different masses have been presented. This gives an indication of the effect of the mass on the dynamic force. It is probable that the mass of the wedge will be slightly higher than 2000 kg.

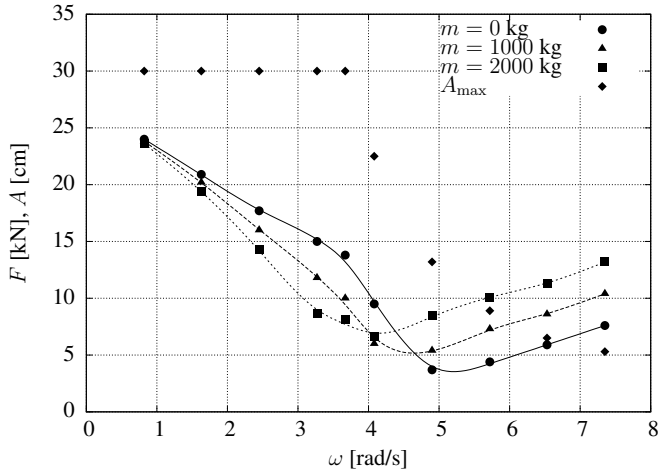

Figure 9: The absolute value of the maximum dynamic force with the maximum motion amplitude. Results for 11 metre long wedge with water line breadth 1.5×575 mm.

The maximum force for the estimated mass occurs for the lowest frequency. This is caused by the dominating buoyancy force. As the frequency increases the maximum force decreases due to the increasing inertia force acting opposite to the buoyancy force. At the same time the damping force increases. By analysing the system in more detail as a dampened mass-spring system, it can be seen that a very rapid phase shift occurs between 4 to 6 rad/s. If the mass is increased the shift occurs at a lower frequency and is more subtle. For higher frequencies the inertia force dominates. However, as the motion amplitude has to be restricted to avoid wave breaking, the maximum force grows rather slowly. It is beneficial to increase the mass of the wave maker at low frequencies, whereas at higher frequencies additional mass increases the maximum dynamical force due to the dominating inertia force.

CONCLUSIONS

Unstructured finite volume method has been verified and used for the design of a plunger type wave maker. The presented work has consisted of two parts.

In the first part the method of manufactured solutions has been used for the verification of a time accurate, surface tracking, free surface flow solver. The bulk flow and time accurate free surface discretisations have been verified separately using two different manufactured solutions. The study has shown that the method of manufactured solutions can be used easily and effectively also for the verification of surface tracking free surface discretisations, i.e. with a highly nonlinear boundary condition.

The results show that the spatial discretisations of the bulk flow for both the velocities and pressure are second order accurate, which is the expected order. Similarly, the free

surface discretisation shows expected order of accuracy and the method is thus verified for the options used in the study.

In the second part of the work the method has been used for the design of a plunger type wave maker. Here, three different triangular wedge angles (25, 35 and 45 degrees) for a plunger type wave maker have been compared in terms of the height and quality of the generated wave. The quality has been assessed by comparing the fluctuations of the vertical and horizontal asymmetries of the wave profiles. Considerable differences have been found both for the generated wave height as well as for the wave quality. Increasing wedge angle leads to higher waves, but it also leads to increased fluctuations of the vertical asymmetry. Additionally, it has been observed that the amplitude of the asymmetry fluctuations is highly dependent on the motion frequency. There seems to be an optimal frequency for each wedge, which increases with increasing wedge angle.

Based on its performace, the 35 degree wedge has been chosen for the new wave maker. A Fourier analysis of the hydrodynamic force combined with wave breaking and mechanical limitations on the motion amplitude has then been used to estimate the maximum force required from the driving mechanism. This same information has also been used for the structural design of the wave maker wedge.

References

Batina, J. T., 'Unsteady euler algorithm with unstructured dynamic mesh for complex-aircraft aerodynamic analysis', AIAA Journal, vol. 29, no. 3, pp. 327–333, 1991.

Caretto, L. S., Gosman, A. D., Patankar, S. V. and Spalding, D. B., 'Two calculation procedures for steady, three-dimensional flows with recirculation', in Proc. Third Int. Conf. Numer. Methods Fluid Dyn., Paris, 1972.

Davidson, L., 'A pressure correction method for unstructured meshes with arbitrary control volumes', International Journal for Numerical Methods in Fluids, vol. 22, pp. 265–281, 1996.

Demirdžić, I. and Muzaferija, S., 'Numerical method for coupled fluid flow, heat transfer and stress analysis using unstructured moving meshes with cells of arbitrary topology', Computer methods in applied mechanics and engineering, vol. 125, pp. 235–255, 1995.

van Doormal, J. and Raithby, G., 'Enhancements of the SIMPLE method for predicting incompressible fluid flows', Numerical Heat Transfer, vol. 7, pp. 147–163, 1984.

Eça, L. and Hoekstra, M., 'On the influence of the iterative error in the numerical uncertainty of ship viscous flow calculations', in 26^{th} Symposium on Naval Hydrodynamics, Rome, Italy, 2006.

Farhat, C., Degand, C., Koobus, B. and Lesoinne, M., 'Torsional springs for two-dimensional dynamic unstructured fluid meshes', Computer methods in applied mechanics and engineering, vol. 163, pp. 231–245, 1998.

Golub, G. and van Loan, C., Matrix computations, Johns Hopkins University Press, Baltimore, 1990.

Granholm, G., Aallonkehittimen teoria ja mallikokeet, Master's thesis, Helsinki University of Technology, 1990, in Finnish.

Hino, T., Martinelli, L. and Jameson, A., 'A finite-volume method with unstructured grid for free surface flow simulations', in 6^{th} International Conference on Numerical Ship Hydrodynamics, Iowa, 1993.

Hoffren, J., 'Unsteady Navier-Stokes simulations of airfoil flows', in Taylor, C., ed., Numerical Methods in Laminar and Turbulent Flow, vol. VIII, pp. 1065–1076, Pineridge Press, 1993.

Mikkola, T., 'On time accurate kinematic boundary condition in surface tracking context', in Bertram, V. and Kyulevcheliev, S., eds., 8^{th} Numerical Towing Tank Symposium, Varna, Bulgaria, 2005.

Mikkola, T., 'Time accurate simulation of a plunger type wave maker using unstructured finite volume solver with surface tracking', in 26^{th} Symposium on Naval Hydrodynamics, Rome, Italy, 2006.

Mikkola, T., 'Verification of a free surface code with method of manufactured solutions', in Bertram, V., ed., 10^{th} Numerical Towing Tank Symposium, Hamburg, Germany, 2007.

Müller, J.-D., On triangles and flow, Ph.D. thesis, University of Michigan, 1996.

Méhauté, B. L., An introduction to hydrodynamics & water waves, Springer-Verlag, 1976.

Paterson, A., A First Course in Fluid Dynamics, Cambridge University Press, 1983.

Raven, H. C., van der Ploeg, A. and Starke, B., 'Computation of free-surface viscous flows at model and full scale by a steady iterative approach', in 25^{th} Symposium on Naval Hydrodynamics, St. John's, Canada, 2004.

Rhie, C. M. and Chow, W. L., 'A numerical study of the turbulent flow past an isolated airfoil with trailing edge separation', AIAA Journal, vol. 21, pp. 1525–1532, 1983.

Roache, P., Verification and Validation in Computational Science and Engineering, Hermosa Publishers, Albuquerque NM, 1998.

Roache, P., 'Code verification by the method of manufactured solutions', Journal of Fluids Engineering, vol. 124, 2002.

Salari, K. and Knupp, P., Code verification by the method of manufactured solutions, Tech. Rep. SAND2000-1444, Sandia National Laboratories, 2000.

Steinberg, S. and Roache, P., 'Symbolic manipulation and computational fluid dynamics', Journal of Computational Physics, vol. 57, no. 2, 1985.

van den Vorst, H. and Sonneveld, P., CGSTAB, a more smoothly converging variant of CGS, Tech. Rep. 90-50, Delft University of Technology, 1990.

Wu, Y.-C., 'Plunger-type wavemaker theory', Journal of Hydraulic Research, vol. 26, no. 4, 1988.

Tommi Mikkola, teaching researcher

Helsinki University of Technology, Ship Laboratory, Tietotie 1, 02015 TKK, Finland
E-mail: tommi.mikkola@tkk.fi